condensed matter

MDPI

Communication

Common Phase and Structure Misidentifications in High-Resolution TEM Characterization of Perovskite Materials

Yu-Hao Deng

Academy for Advanced Interdisciplinary Studies, Peking University, Beijing 100871, China; yuhaodeng@pku.edu.cn

Abstract: High-resolution TEM (HRTEM) is a powerful tool for structure characterization. However, methylammonium lead iodide ($MAPbI_3$) perovskite is highly sensitive to electron beams and easily decomposes into lead iodide (PbI_2). Misidentifications, such as PbI_2 being incorrectly labeled as perovskite, are widely present in HRTEM characterization and would negatively affect the development of perovskite research field. Here misidentifications in $MAPbI_3$ perovskite are summarized, classified, and corrected based on low-dose imaging and electron diffraction (ED) simulations. Corresponding crystallographic parameters of intrinsic tetragonal $MAPbI_3$ and the confusable hexagonal PbI_2 are presented unambiguously. Finally, the method of proper phase identification and some strategies to control the radiation damage in HRTEM are provided. This warning paves the way to avoid future misinterpretations in HRTEM characterization of perovskite and other electron beam-sensitive materials.

Keywords: $MAPbI_3$ perovskite; transmission electron microscopy (TEM); electron diffraction (ED); phase identification; electron beam-sensitive

Citation: Deng, Y.-H. Common Phase and Structure Misidentifications in High-Resolution TEM Characterization of Perovskite Materials. *Condens. Matter* **2021**, *6*, 1. https://doi.org/10.3390/condmat6010001

Received: 5 October 2020
Accepted: 25 December 2020
Published: 29 December 2020

1. Introduction

High-resolution transmission electron microscopy (HRTEM) is a powerful characterization tool and has been extensively and successfully used for analyzing crystal structures on an atomic scale [1–4]. Recently, halide perovskites have achieved substantial success in various optoelectronic devices owing to their solution-based growth and their remarkable physical properties [5–9]. However, the extensively studied methylammonium lead iodide ($MAPbI_3$) perovskite is very sensitive to electron beam irradiation. Figure 1 shows the $MAPbI_3$ degradation process under electron beam irradiation. Tetragonal perovskite decomposes into hexagonal lead iodide (PbI_2) by the dissociation of methylamine and hydrogen iodide molecules.

Comparing distances and angles between crystal planes to identify the material phase, it is easy to ignore the missing crystal planes, which leads to false identification results, such as labelling lead iodide as perovskite. In a proper phase identification, HRTEM images alone cannot be used for phase identification, but always have to be supported by other measurement results such as diffractograms, simulated ED, nanodiffractions, or XRD specimen data [1]. As a rough estimation, $MAPbI_3$ decomposes into PbI_2 at a total dose irradiation > 150 $eÅ^{-2}$ [10,11]. However, the value of the electron dose in normal HRTEM is around 800–2000 $eÅ^{-2}$ s^{-1}, so the experimental total dose would have been much higher than the critical dose of $MAPbI_3$ perovskite. Meanwhile, distances and angles between crystal planes in the decomposition product PbI_2 are very similar to $MAPbI_3$, such that PbI_2 can easily be misidentified as perovskite. A typical feature of such misidentification is missing crystal planes in the results. Therefore, the absence of crystal planes serves as an indicator that the material is not in the perovskite, but another structural phase.

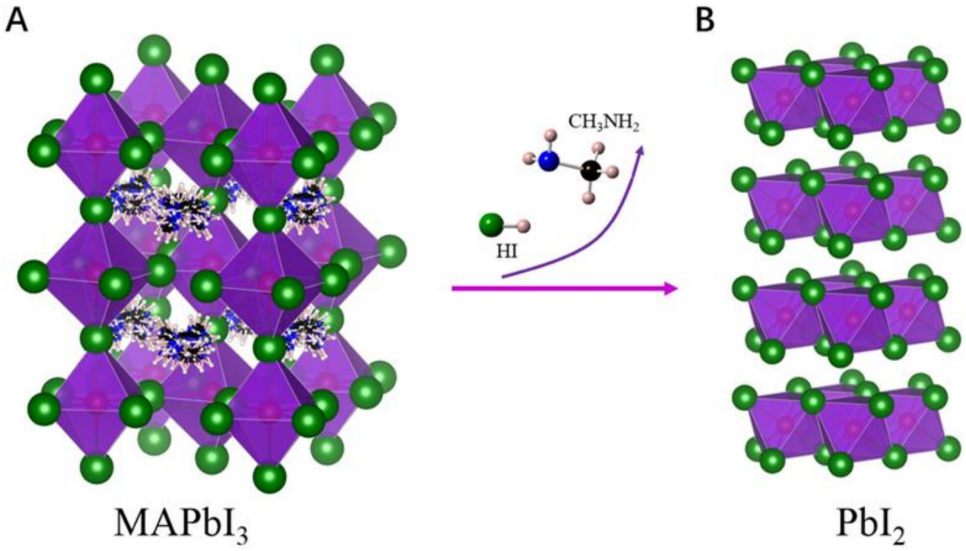

Figure 1. $MAPbI_3$ degradation under electron beam irradiation. Tetragonal perovskite (**A**) decomposes into hexagonal lead iodide (**B**) via dissociation of methylamine and hydrogen iodide molecules. Here, colors represent the following: green, iodine; red, lead; black, carbon; blue, nitrogen; pink, hydrogen.

Such misidentifications were widely ignored in literature studies [9,12–31]. Figure 2 shows typical HRTEM images with missing crystal planes. $(1\bar{1}0)$, (002) planes are missing along the [110] zone axis (Figure 2A) [21], (020) plane is missing along the [101] zone axis (Figure 2B) [27], $(11\bar{2})$, (112) planes are missing along the $[\bar{2}01]$ zone axis (Figure 2C) [13], and (002) plane is missing along the $[\bar{1}20]$ zone axis (Figure 2D) [28]. However, missing crystal planes have been observed in low-dose imaging. Thus far, Song et al. have observed the missing $(1\bar{1}0)$, (002) planes with 0.63 nm along [110] zone axis at total doses of 1.5 $e\text{Å}^{-2}$ (Figure 3A) [32]. Similarly, Zhu et al. have observed the missing $(1\bar{1}2)$, (112) planes with 0.44 nm along the $[\bar{2}01]$ zone axis by Cryo-TEM at a low electron dose of about 3 e Å^{-2} (Figure 3B) [33]. Moreover, the missing crystal planes have also been observed in other characterization techniques based on the Bragg's law, such as selected area electron diffraction (SEAD) (Figure 3C) [34] and X-ray diffraction (XRD) (Figure 3D) [10,35–37]. Finally, the low-order crystal plane (d(112) = 4.4 Å) has longer interplanar spacing than the high-order crystal plane (d(224) = 2.2 Å). Thus, the missing of low-order crystal planes should not result from the poor accuracy in the data interpretation. Although the mistakes are taken seriously [10,11,35], an urgently needed, complete summary and correction of that issue has not been published yet.

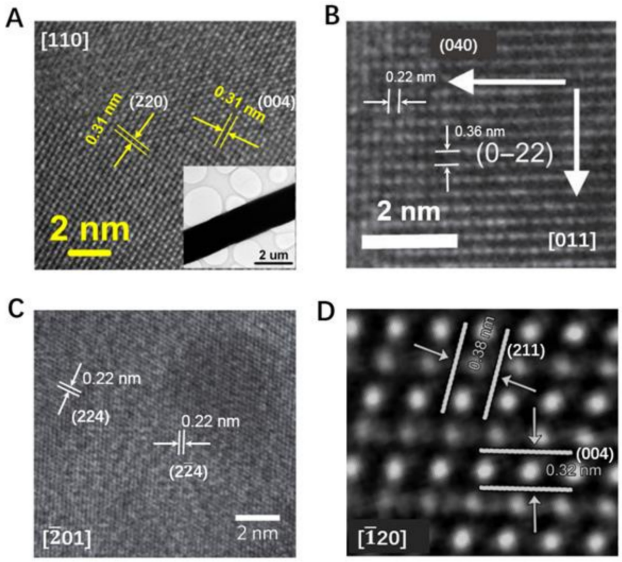

Figure 2. Typical HRTEM images with missing crystal planes. (**A**) $(1\bar{1}0)$, (002) planes are missing along the [110] zone axis. (**B**) (020) plane is missing along the [101] zone axis (Figure 2B). (**C**) $(11\bar{2})$, (112) planes are missing along the $[\bar{2}01]$ zone axis. (**D**) (002) plane is missing along the $[\bar{1}20]$ zone axis. (**A**) Reprinted with permission from Ref. [21], © American Chemical Society 2016. (**B**) Reproduced with permission from Ref. [27]. (**C**) Reprinted by permission from Springer Customer Service Centre GmbH: Springer Nature, Nature Photonics Gong et al., Highly efficient quantum dot near-infrared light-emitting diodes, © 2016. (**D**) Reproduced with permission from Ref. [28], © WILEY-VCH Verlag GmbH & Co. KGaA, Weinheim, Germany, 2015.

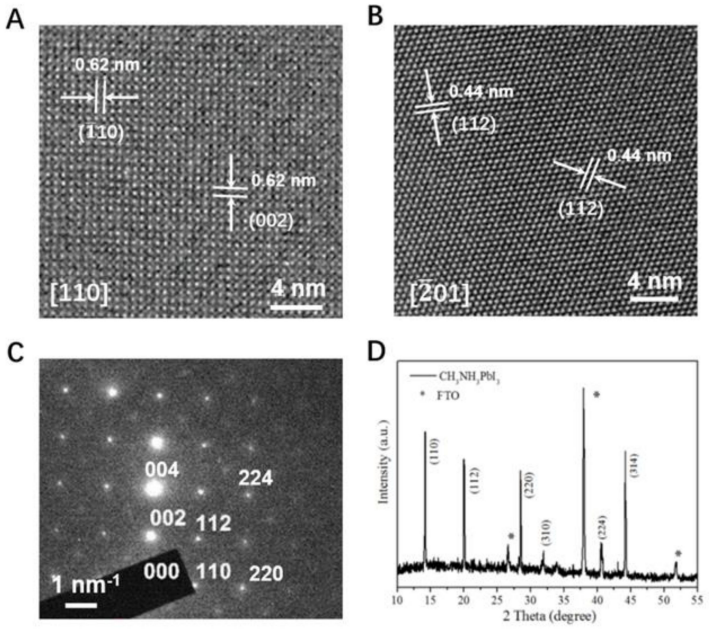

Figure 3. Intrinsic $MAPbI_3$ with complete crystal planes. (**A**) $(1\bar{1}0)$, (002) planes along [110] zone axis were observed at total doses of 1.5 eÅ-2. (**B**) $(11\bar{2})$, (112) planes along the $[\bar{2}01]$ zone axis were observed by Cryo-TEM at a low electron dose of about 3 e Å-2. (**C**) Selected area electron diffraction (SEAD) of $MAPbI_3$ perovskite. (**D**) X-ray diffraction (XRD) of $MAPbI_3$ perovskite. (**A**) Reproduced with permission from Ref. [32], © WILEY-VCH Verlag GmbH & Co. KGaA, Weinheim, Germany, 2020. (**B**) Reproduced with permission from Ref. [33], © 2020 Elsevier B.V. 2020. (**C**) Reproduced with permission from Ref. [34], © WILEY-VCH Verlag GmbH & Co. KGaA, Weinheim, Germany, 2018. (**D**) Reproduced with permission from Ref. [10], © Springer Nature 2018.

2. Results and Discussion

Here misidentifications in $MAPbI_3$ perovskite are summarized, classified and corrected. Figure 4 shows simulated ED patterns of $MAPbI_3$ and PbI_2 along different axis zones. Figure 4A is the ED pattern of $MAPbI_3$ along [110] zone axis. $(\bar{1}10)$, (002) crystal planes are present in intrinsic tetragonal perovskite, but they are missing in a number of HRTEM characterizations [12–15]. Figure 4B shows the simulated ED patterns of PbI_2 along $[4\bar{4}1]$ zone axis. (014), $(\bar{1}04)$ crystal planes of PbI_2 have the similar distances and angles between crystal planes compared to $(\bar{2}20)$, (004) crystal planes of $MAPbI_3$. In the actual experiment, $MAPBI_3$ would decompose into PBI_2 and the missing crystal planes would be oftentimes ignored, leading to aforementioned mischaracterizations. Similarly, Figure 4C–H show ED patterns of $MAPbI_3$ along [101] and PbI_2 along [8 10 1], $MAPbI_3$ along $[\bar{2}01]$ and PbI_2 along $[8\bar{8}1]$, $MAPbI_3$ along $[\bar{1}20]$ and PbI_2 along $[\bar{4}11]$, respectively. The missing crystal planes in HRTEM characterizations are indicated by red circles in Figure 4.

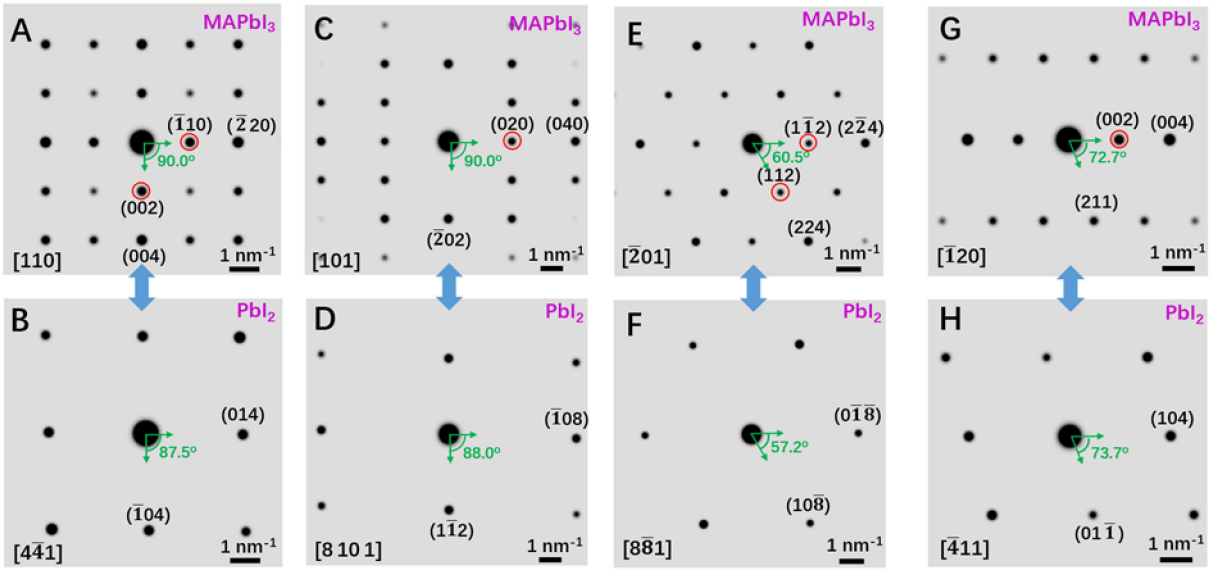

Figure 4. Simulated electron diffraction (ED) patterns of tetragonal $MAPbI_3$ and hexagonal PbI_2. (**A**) $MAPbI_3$ along [110] axis zone. (**B**) PbI_2 along $[4\bar{4}1]$ zone axis. (**C**) $MAPbI_3$ along [101] axis zone. (**D**) PbI_2 along [8 10 1] zone axis. (**E**) $MAPbI_3$ along $[\bar{2}01]$ zone axis. (**F**) PbI_2 along $[8\bar{8}1]$ zone axis. (**G**) $MAPbI_3$ along $[\bar{1}20]$ zone axis. (**H**) PbI_2 along $[\bar{4}11]$ zone axis. Crystal planes marked in red circle are missing in published articles [9,12–31].

Misidentifications exist in the following fields: phase identification and structure determination [16], grain, nanowire, and microwire orientation [9,14,17–19], morphology analysis and shape control of nanocrystals [20], growth direction of perovskite materials [21], degradation process and kinetics of perovskite [22], phase transition research in perovskite [26], and ion migration characterization in photoelectric devices [27]. Misidentifications not only occur in single component materials, but also in heterostructures, such as lattice matching and kinetic study in epitaxial growth of perovskite films on 2D materials [25], PbS quantum dots in perovskite materials [12,13], and lattice-anchoring stabilized perovskite research [14]. HRTEM is an auxiliary tool to identify the phase of perovskite materials and misinterpretations would not influence their device performances and conclusions. However, in some cases, such as the growth direction, orientation, and lattice matching of perovskite materials, misinterpretations in HRTEM would result in wrong conclusions. To make the comparisons and corrections clearer, Table 1 shows the detailed parameters of the intrinsic $MAPbI_3$ and confusable PbI_2 along different zone axis, where missing crystal planes are marked in red. Remarkably, the [110] and [001] zone axes are equivalent in tetragonal $MAPbI_3$ perovskite.

Table 1. Detailed crystallographic parameters of $MAPbI_3$ and PbI_2 along different zone axes corresponding to Figure 4, the missing low-order crystal planes of $MAPbI_3$ are marked in red. The similar crystal angles and interplanar spacings make them to be easily confused.

Material and Zone Axis	Characteristic Crystal Planes	Interplanar Spacing	Interplanar Angle	References
$MAPbI_3$ [110]	$(\bar{1}10)$, $(\bar{2}20)$ (002), (004)	d$(\bar{1}10)$ = 6.2Å. d$(\bar{2}20)$ = 3.1Å. d(002) = 6.3Å. d(004) = 3.2Å.	<$(\bar{1}10)$, (002)> =<$(\bar{2}20)$, (004)> = 90.0°	[9,15–25]
PbI_2 [$4\bar{4}1$]	(014) $(\bar{1}04)$	d(014) = 3.2Å .d$(\bar{1}04)$ = 3.2Å.	<(014), $(\bar{1}04)$> = 87.5°	_____
$MAPbI_3$ [101]	(020), (040) $(\bar{2}02)$	d(020) = 4.4Å. d(040) = 2.2Å. d$(\bar{2}02)$ = 3.6Å.	<(020), $(\bar{2}02)$> =<(040), $(\bar{2}02)$> =90.0°	[26,27]
PbI_2 [8 10 1]	$(\bar{1}08)$ $(1\bar{1}2)$	d$(\bar{1}08)$ = 2.2Å. d$(1\bar{1}2)$ = 3.7Å.	<$(\bar{1}08)$, $(1\bar{1}2)$> = 88.0°	_____
$MAPbI_3$ [$\bar{2}01$]	$(1\bar{1}2)$, $(2\bar{2}4)$ (112), (224)	d$(1\bar{1}2)$ = 4.4Å. d$(2\bar{2}4)$ = 2.2Å. d(112) = 4.4Å. d(224) = 2.2Å.	<$(1\bar{1}2)$, (112)> =<$(2\bar{2}4)$, (224)> = 60.5°	[12–14,18]
PbI_2 [$8\bar{8}1$]	$(0\bar{1}\,\bar{8})$ $(10\bar{8})$	d$(0\bar{1}\,\bar{8})$ = 2.2Å. d$(10\bar{8})$ = 2.2Å.	<$(0\bar{1}8)$, $(10\bar{8})$> = 57.2°	_____
$MAPbI_3$ [$\bar{1}20$]	(002), (004) (211)	d(002) = 6.3Å. d(004) = 3.2Å. d(211)= 3.8Å.	<(002), (211)> =<(004), (211)> = 72.7°	[28–31]
PbI_2 [$\bar{4}11$]	(104) $(01\bar{1})$	d(104) = 3.2Å. d$(01\bar{1})$ = 3.9Å.	<(104), $(01\bar{1})$> = 73.7°	_____

The $MAPbI_3$ perovskite is extremely beam-sensitive with a critical dose around a few hundred electrons per square angstrom. For most measurements, and in particular HRTEM, keeping the dose below the critical value is extremely challenging [38–40]. However, there are some ways to reduce the radiation damage in HRTEM, which might be helpful in obtaining the intrinsic structure of perovskite materials. Low-dose imaging techniques are effective approaches for electron beam-sensitive materials [41]. Zhang et al. developed a program to achieve a direct, one-step alignment of the zone axis and obtained HRTEM images of electron beam-sensitive materials with a dose of 6–12 e $Å^{-2}$ [42]. Carlino reported the in-line holography in TEM for the study of radiation-sensitive materials providing high-contrast holograms within 1–2 e$Å^{-2}s^{-1}$ [43]. The intrinsic structure of $MAPbI_3$ has been captured by the Direct-detection electron-counting (DDEC) cameras at doses below 3 e $Å^{-2}$ [33,44]. Cooling the specimen also poses a feasible way to reduce damage. Using Cryo-TEM, HRTEM images of $MAPbI_3$ has been captured [11,33]. Lastly, encapsulation of specimen with a thin, stable, and continuous layer reduces radiation damage [40]. In any case, the total electron dose should be below the critical dose of $MAPbI_3$, otherwise substantial damage occurs during TEM characterizations.

3. Conclusions

The $MAPbI_3$ perovskite is very sensitive to electron beam irradiation and easily decomposes into PbI_2. HRTEM characterizations performed above the critical dose can easily lead to misinterpretations, falsely identifying decomposition products as the actual perovskite. An indicator of such confusable decomposition products is missing crystal planes when comparing the expected theoretical diffractograms to the actual experimental data of $MAPbI_3$. The summarized and analyzed misidentifications in HRTEM characterization of $MAPbI_3$ may be helpful for researchers to avoid such misidentifications in perovskite research. Our findings show that it is unreliable to identify material phases only by measur-

ing distances and angles between crystal planes. We need to take diffractograms, simulated ED, nanodiffractions, or XRD data into consideration in order to ensure complete crystal planes. We also provide a method of proper phase identification and some strategies to reduce the radiation damage in HRTEM.

4. Methods

Corresponding crystal structures cif files were downloaded from Crystallography Open Database (COD) website. COD IDs of $MAPbI_3$ and PbI_2 are 4124388 and 9009141 respectively [45,46]. $MAPbI_3$ is I4/mcm space group with tetragonal structure, cell parameters: a = b = 8.839Å, c = 12.695Å; $\alpha = \beta = \gamma = 90^\circ$. PbI_2 is P-3m1 space group with hexagonal structure, cell parameters: a = b = 4.555Å, c = 20.937Å; $\alpha = \beta = 90^\circ$, $\gamma = 120^\circ$. The electron diffraction (ED) simulations of $MAPbI_3$ and PbI_2 were obtained using CrystalMaker Software. The interplanar spacings and interplanar angles can be calculated from the cell parameters. During the process of phase identification, we also tried other polytypes of PbI_2, but the results did not match well.

Funding: This research received no external funding.

Data Availability Statement: All data are available from the corresponding author upon reasonable request.

Acknowledgments: The authors thank anonymous reviewers, academic editors and Leon Georg Nest for helpful suggestions and assistant editors for communications. The authors also appreciate the encouragements from Ying Xiong, Shulin Chen and Leon Georg Nest.

Conflicts of Interest: The author declares no competing financial interest.

References

1. Spence, J.C.H. *High-Resolution Electron Microscopy*; OUP Oxford: Oxford, UK, 2013.
2. Jia, C.L.; Lentzen, M.; Urban, K. Atomic-resolution imaging of oxygen in perovskite ceramics. *Science* **2003**, *299*, 870–873. [CrossRef] [PubMed]
3. Pennycook, S.J.; Li, C.; Li, M.; Tang, C.; Okunishi, E.; Varela, M.; Kim, Y.-M.; Jang, J.H. Material structure, properties, and dynamics through scanning transmission electron microscopy. *J. Anal. Sci. Technol.* **2018**, *9*, 11. [CrossRef]
4. Krivanek, O.; Chisholm, M.F.; Nicolosi, V.; Pennycook, T.J.; Corbin, G.J.; Dellby, N.; Murfitt, M.F.; Own, C.S.; Szilagyi, Z.S.; Oxley, M.P.; et al. Atom-by-atom structural and chemical analysis by annular dark-field electron microscopy. *Nature* **2010**, *464*, 571–574. [CrossRef] [PubMed]
5. Best Research-Cell Efficiencies. National Renewable Energy Laboratory. Available online: https://www.nrel.gov/pv/cell-efficiency.html (accessed on 15 October 2020).
6. Lin, K.; Xing, J.; Na Quan, L.; De Arquer, F.P.G.; Gong, X.; Lu, J.; Xie, L.; Zhao, W.; Zhang, D.; Yan, C.; et al. Perovskite light-emitting diodes with external quantum efficiency exceeding 20 per cent. *Nature* **2018**, *562*, 245–248. [CrossRef] [PubMed]
7. Yang, Z.; Deng, Y.; Zhang, X.; Wang, S.; Chen, H.; Yang, S.; Khurgin, J.; Fang, N.X.; Zhang, X.; Ma, R.-M. High-Performance Single-Crystalline Perovskite Thin-Film Photodetector. *Adv. Mater.* **2018**, *30*, 1704333. [CrossRef]
8. Deng, Y.H.; Yang, Z.Q.; Ma, R.M. Growth of centimeter-scale perovskite single-crystalline thin film via surface engineering. *Nano Converg.* **2020**, *7*, 1–7. [CrossRef]
9. Zhu, H.; Fu, Y.; Meng, F.; Wu, X.; Gong, Z.; Ding, Q.; Gustafsson, M.V.; Trinh, M.T.; Jin, S.; Zhu, X.-Y. Lead halide perovskite nanowire lasers with low lasing thresholds and high quality factors. *Nat. Mater.* **2015**, *14*, 636–642. [CrossRef]
10. Chen, S.; Zhang, X.; Zhao, J.; Zhang, Y.; Kong, G.; Li, Q.; Li, N.; Yu, Y.; Xu, N.; Zhang, J.; et al. Atomic scale insights into structure instability and decomposition pathway of methylammonium lead iodide perovskite. *Nat. Commun.* **2018**, *9*, 1–8.
11. Li, Y.; Zhou, W.; Li, Y.; Huang, W.; Zhang, Z.; Chen, G.; Wang, H.; Wu, G.-H.; Rolston, N.; Vila, R.; et al. Unravelling degradation mechanisms and atomic structure of organic-inorganic halide perovskites by cryo-EM. *Joule* **2019**, *3*, 2854–2866. [CrossRef]
12. Ning, Z.; Gong, X.; Comin, R.; Walters, G.; Fan, F.; Voznyy, O.; Yassitepe, E.; Buin, A.K.; Hoogland, S.; Sargent, E.H. Quantum-dot-in-perovskite solids. *Nature* **2015**, *523*, 324–328. [CrossRef]
13. Gong, X.; Yang, Z.; Walters, G.; Comin, R.; Ning, Z.; Beauregard, E.; Adinolfi, V.; Voznyy, O.; Sargent, E.H. Highly efficient quantum dot near-infrared light-emitting diodes. *Nat. Photonics* **2016**, *10*, 253–257. [CrossRef]
14. Liu, M.; Chen, Y.; Tan, C.-S.; Quintero-Bermudez, R.; Proppe, A.H.; Munir, R.; Tan, H.; Voznyy, O.; Scheffel, B.; Walters, G.; et al. Lattice anchoring stabilizes solution-processed semiconductors. *Nature* **2019**, *570*, 96–101. [CrossRef] [PubMed]
15. Son, D.-Y.; Lee, J.-W.; Choi, Y.J.; Jang, I.-H.; Lee, S.; Yoo, P.J.; Shin, H.; Ahn, N.; Choi, M.; Kim, D.; et al. Self-formed grain boundary healing layer for highly efficient CH 3 NH 3 PbI 3 perovskite solar cells. *Nat. Energy* **2016**, *1*, 1–8.

16. Yang, M.; Zhou, Y.; Zeng, Y.; Jiang, C.; Padture, N.P.; Zhu, K. Square-centimeter solution-processed planar $CH_3NH_3PbI_3$ perovskite solar cells with efficiency exceeding 15%. *Adv. Mater.* **2015**, *27*, 6363–6370. [CrossRef] [PubMed]
17. Xiao, M.; Huang, F.; Huang, W.; Dkhissi, Y.; Zhu, Y.; Etheridge, J.; Gray-Weale, A.; Bach, U.; Cheng, Y.-B.; Spiccia, L. A fast deposition-crystallization procedure for highly efficient lead iodide perovskite thin-film solar cells. *Angew. Chem. Int. Ed.* **2014**, *53*, 9898–9903. [CrossRef]
18. Yang, B.; Dyck, O.; Poplawsky, J.; Keum, J.; Das, S.; Puretzky, A.; Aytug, T.; Joshi, P.C.; Rouleau, C.M.; Duscher, G.; et al. Controllable Growth of Perovskite Films by Room-Temperature Air Exposure for Efficient Planar Heterojunction Photovoltaic Cells. *Angew. Chem. Int. Ed.* **2015**, *54*, 14862–14865. [CrossRef]
19. Li, S.; Li, Y.; Shi, Z.; Lei, L.; Ji, H.; Wu, D.; Xu, T.; Li, X.; Du, G. Fabrication of morphology-controlled and highly-crystallized perovskite microwires for long-term stable photodetectors. *Sol. Energy Mater. Sol. Cells* **2019**, *191*, 275–282. [CrossRef]
20. Zhu, F.; Men, L.; Guo, Y.; Zhu, Q.; Bhattacharjee, U.; Goodwin, P.M.; Petrich, J.W.; Smith, E.A.; Vela, J. Shape evolution and single particle luminescence of organometal halide perovskite nanocrystals. *ACS Nano* **2015**, *9*, 2948–2959. [CrossRef]
21. Gao, L.; Zeng, K.; Guo, J.; Ge, C.; Du, J.; Zhao, Y.; Chen, C.; Deng, H.; Haisheng, S.; Song, H.; et al. Passivated single-crystalline $CH_3NH_3PbI_3$ nanowire photodetector with high detectivity and polarization sensitivity. *Nano Lett.* **2016**, *16*, 7446–7454. [CrossRef]
22. Fan, Z.; Xiao, H.; Wang, Y.; Zhao, Z.; Lin, Z.; Cheng, H.-C.; Lee, S.-J.; Wang, G.; Feng, Z.; Goddard, I.W.A.; et al. Layer-by-layer degradation of methylammonium lead tri-iodide perovskite microplates. *Joule* **2017**, *1*, 548–562. [CrossRef]
23. Li, D.; Wang, G.; Cheng, H.-C.; Chen, C.-Y.; Wu, H.; Liu, Y.; Huang, Y.; Duan, X. Size-dependent phase transition in methylammonium lead iodide perovskite microplate crystals. *Nat. Commun.* **2016**, *7*, 1–8. [CrossRef] [PubMed]
24. Kim, S.; Bae, S.; Lee, S.-W.; Cho, K.; Lee, K.D.; Kim, H.; Park, S.; Kwon, G.; Ahn, S.-W.; Lee, H.-M.; et al. Relationship between ion migration and interfacial degradation of $CH_3NH_3PbI_3$ perovskite solar cells under thermal conditions. *Sci. Rep.* **2017**, *7*, 1–9. [CrossRef] [PubMed]
25. Tang, G.; You, P.; Tai, Q.; Yang, A.; Cao, J.; Zheng, F.; Zhou, Z.; Zhao, J.; Chan, P.K.L.; Yan, F. Solution-Phase Epitaxial Growth of Perovskite Films on 2D Material Flakes for High-Performance Solar Cells. *Adv. Mater.* **2019**, *31*, 1807689. [CrossRef] [PubMed]
26. Kim, T.W.; Uchida, S.; Matsushita, T.; Cojocaru, L.; Jono, R.; Kimura, K.; Matsubara, D.; Shirai, M.; Ito, K.; Matsumoto, H.; et al. Self-Organized Superlattice and Phase Coexistence inside Thin Film Organometal Halide Perovskite. *Adv. Mater.* **2018**, *30*, 1705230. [CrossRef]
27. Wang, G.; Li, D.; Cheng, H.C.; Li, Y.; Chen, C.-Y.; Yin, A.; Zhao, Z.; Lin, Z.; Wu, H.; He, Q.; et al. Wafer-scale growth of large arrays of perovskite microplate crystals for functional electronics and optoelectronics. *Sci. Adv.* **2015**, *1*, e1500613. [CrossRef] [PubMed]
28. Niu, L.; Liu, X.; Cong, C.; Wu, C.; Wu, D.; Chang, T.R.; Wang, H.; Zeng, Q.; Zhou, J.; Wang, X.; et al. Controlled synthesis of organic/inorganic Van der waals solid for tunable light–matter interactions. *Adv. Mater.* **2015**, *27*, 7800–7808. [CrossRef] [PubMed]
29. Liu, X.; Niu, L.; Wu, C.; Cong, C.; Wang, H.; Zeng, Q.; He, H.; Fu, Q.; Fu, W.; Yu, T.; et al. Periodic Organic–Inorganic Halide Perovskite Microplatelet Arrays on Silicon Substrates for Room-Temperature Lasing. *Adv. Sci.* **2016**, *3*, 1600137. [CrossRef]
30. Kim, T.W.; Shibayama, N.; Cojocaru, L.; Uchida, S.; Kondo, T.; Segawa, H. Real-time in situ observation of microstructural change in organometal halide perovskite induced by thermal degradation. *Adv. Funct. Mater.* **2018**, *28*, 1804039. [CrossRef]
31. Zhao, J.; Kong, G.; Chen, S.; Li, Q.; Huang, B.; Liu, Z.; San, X.; Wang, Y.; Wang, C.; Zhen, Y.; et al. Single crystalline $CH_3NH_3PbI_3$ self-grown on FTO/TiO_2 substrate for high efficiency perovskite solar cells. *Sci. Bull.* **2017**, *62*, 405–418. [CrossRef]
32. Song, K.; Liu, L.; Zhang, D.; Hautzinger, M.P.; Jin, S.; Han, Y. Atomic-Resolution Imaging of Halide Perovskites Using Electron Microscopy. *Adv. Energy Mater.* **2020**, *10*, 1904006. [CrossRef]
33. Zhu, Y.; Guia, Z.; Wang, Q.; Meng, F.; Feng, S.; Han, B.; Wang, P.; Huang, L.; Wang, H.-L.; Gu, M.; et al. Direct atomic scale characterization of the surface structure and planar defects in the organic-inorganic hybrid $CH_3NH_3PbI_3$ by Cryo-TEM. *Nano Energy* **2020**, *73*, 104820. [CrossRef]
34. Rothmann, M.U.; Li, W.; Zhu, Y.; Liu, A.; Ku, Z.; Bach, U.; Etheridge, J.; Cheng, Y. Structural and chemical changes to $CH_3NH_3PbI_3$ induced by electron and gallium ion beams. *Adv. Mater.* **2018**, *30*, 1800629. [CrossRef] [PubMed]
35. Dong, Q.; Fang, Y.; Shao, Y.; Mulligan, P.; Qiu, J.; Cao, L.; Huang, J. Electron-hole diffusion lengths 175 μm in solution-grown $CH_3NH_3PbI_3$ single crystals. *Science* **2015**, *347*, 967–970. [CrossRef] [PubMed]
36. Shi, D.; Adinolfi, V.; Comin, R.; Yuan, M.; Alarousu, E.; Buin, A.K.; Chen, Y.; Hoogland, S.H.; Rothenberger, A.; Katsiev, K.; et al. Low trap-state density and long carrier diffusion in organolead trihalide perovskite single crystals. *Science* **2015**, *347*, 519–522. [CrossRef] [PubMed]
37. Zhang, X.W.; Yang, Z.Q.; Li, J.Z.; Deng, Y.H.; Hou, Y.M.; Mao, Y.F.; Lu, J.; Ma, R.M. Directly imaging the structure–property correlation of perovskites in crystalline microwires. *J. Mater. Chem. A* **2019**, *7*, 13305–13314. [CrossRef]
38. Egerton, R.F. Outrun radiation damage with electrons? *Adv. Struct. Chem. Imaging* **2015**, *1*, 1–11. [CrossRef]
39. Egerton, R.F. Control of radiation damage in the TEM. *Ultramicroscopy* **2013**, *127*, 100–108. [CrossRef]
40. Egerton, R.F. Radiation damage to organic and inorganic specimens in the TEM. *Micron* **2019**, *119*, 72–87. [CrossRef]
41. Egerton, R.F.; Qian, H. Exploiting the Dose-Rate Dependence of Radiolysis–a Future for Cryo-STEM? *Microsc. Microanal.* **2019**, *25*, 992–993. [CrossRef]
42. Zhang, D.; Zhu, Y.; Liu, L.; Ying, X.; Hsiung, C.-E.; Sougrat, R.; Li, K.; Han, Y. Atomic-resolution transmission electron microscopy of electron beam–sensitive crystalline materials. *Science* **2018**, *359*, 675–679. [CrossRef]
43. Carlino, E. In-Line Holography in Transmission Electron Microscopy for the Atomic Resolution Imaging of Single Particle of Radiation-Sensitive Matter. *Materials* **2020**, *13*, 1413. [CrossRef] [PubMed]

44. Chen, S.; Zhang, Y.; Zhao, J.; Mi, Z.; Zhang, J.; Cao, J.; Feng, J.; Zhang, G.; Qi, J.; Li, J.; et al. Transmission electron microscopy of organic-inorganic hybrid perovskites: Myths and truths. *Sci. Bull.* **2020**. [CrossRef]
45. COD of $MAPbI_3$ (4124388). University of Cambridge. Available online: http://www.crystallography.net/cod/4124388.html (accessed on 15 October 2020).
46. COD of PbI_2 (9009141). University of Cambridge. Available online: http://www.crystallography.net/cod/9009141.html (accessed on 15 October 2020).